An application of multiscale early arrival waveform inversion to shallow seismic data

Han Yu[*] and Sherif M. Hanafy

King Abdullah University of Science and Technology, Physical Sciences and Engineering, Thuwal 23955-6900, Saudi Arabia

ABSTRACT

We estimate the near surface velocity distribution by applying multiscale early arrival waveform inversion (MEWI) to shallow seismic land data. This data set is collected at Wadi Qudaid in western Saudi Arabia with the purpose of characterizing the shallow subsurface for its water storage and reuse potential. To enhance the accuracy of MEWI, we correct for the attenuation effects with an estimated factor Q, and also extract a natural source wavelet from the data. We then applied MEWI to invert the processed data for tomograms on different scales starting from a traveltime tomogram as our initial velocity model. Results suggest that, compared to traveltime tomography, MEWI can generate a more highly resolved velocity tomogram from shallow seismic data by inverting its low-frequency components on coarse grids and its high-frequency components on fine grids. The estimated water table in the MEWI tomogram is generally consistent with, but 9% deeper than, the traveltime tomogram, showing that the water storage in this wadi might be less than expected from the traveltime tomogram. We believe that the more accurate MEWI tomogram will make an economically important difference in assessing the storage potential of this wadi and wadis throughout the world.

INTRODUCTION

Traveltime tomography (Zhu and McMechan 1989; Pratt and Goulty 1991; Aki and Richards 2002) is a ray-based geophysical imaging method that inverts the first arrival traveltimes for the subsurface velocity distribution. It iteratively updates the velocity models by smearing the traveltime residuals along the calculated ray paths (Nolet 1987), and provides a smooth estimate of the earth's velocity distribution. However, traveltime tomography employs a high-frequency assumption that conflicts with the finite-frequency bandwidth of seismic data, and so generates tomograms with low-to-intermediate resolution.

Full waveform inversion (FWI) (Tarantola 1984) can overcome the high-frequency limitation in either the space-frequency (Marfurt 1984; Song and Williamson 1995; Pratt, Shin and Hicks 1998) or the space-time domains (Tarantola 1984; Mora 1987; Zhou *et al*. 1995). However, FWI is computationally expensive and its misfit function is highly non-linear with respect to velocity perturbations. Therefore, Sheng *et al*. (2006) proposed an early arrival waveform tomography method in the time-space domain for near surface refraction data. This approach can handle field data if we have a good approximation of the subsurface velocity (Buddenseik 2004), and largely avoids having to account for dominant elastic effects in the data such as surface waves and P-to-S converted reflections. In this method, fewer events need to be fitted than in FWI, but local minima problems usually appear

even if a time window is applied to seismic data. This phenomenon is attributed to high-frequency data used in the inversion, which causes the misfit function to be highly non-linear.

In contrast, multiscale waveform inversion (MWI), proposed by Bunks *et al*. (1995), initially inverts the low-pass filtered data and then gradually incorporates the higher frequencies into the inversion. MWI is more likely to reach global misfit minimum (Sirgue and Pratt 2004) because the misfit function at low frequencies is more linear with respect to slowness perturbations than at high frequencies, and cycle skipping problems are mitigated. Once a smooth or low-wave number tomogram is inverted from data at low frequencies, a higher wave number tomogram can be progressively reconstructed from the data at higher frequencies. A strategy to select optimal frequency bands for different scales is proposed by Sirgue and Pratt (2004).

In this work, our goal is to apply the multiscale early arrival waveform inversion (MEWI) with an attenuation factor to a land data set collected at Wadi Qudaid, 100 km north of Jeddah, Saudi Arabia. Wadis are closely associated with centres of human population because subsurface water is often found and can be extracted by wells. Essential to locating the subsurface water is the precise characterization of the subsurface properties of the wadi. Such properties include the extent of the porous rock in the subsurface, the depth of the impermeable bedrock, and the presence of any faults that might drain the water from the storage reservoir. We propose to characterize the subsurface geology of a wadi by seismic MEWI, a method with much better resolution

---

[*] Han.Yu@kaust.edu.sa

than traditional traveltime tomography (Bunks *et al.* 1995; Zhou *et al.* 1995, 1997; Sirgue and Pratt 2004). Since the subsurface soils are partially to fully saturated, the attenuation factor Q is required to correct for attenuation effects, especially in the data at high frequencies, before we invert for the velocity model. The waveform velocity tomogram is used to delineate the depth to the bedrock and the extent of the overlying porous rock, and therefore estimate the wadi's potential for water storage. A local well log is used to identify porous rock from the seismic velocities in the tomogram.

In this paper, we first present the theory of MEWI. In the following section, we introduce our seismic survey and data processing steps for the wadi data. The MEWI and traveltime tomography methods are applied to the early arrivals of the two-dimensional (2D) land data set, and the resulting tomograms are compared to one another in the numerical results section. The last section summarizes the salient results of our research.

THEORY

Acoustic waveform inversion

Early arrival waveform inversion (EWI) assumes the constant-density acoustic wave equation,

$$\frac{1}{c^2(x)}\frac{\partial^2 p(x,t\,|\,x_s)}{\partial t^2} - \nabla^2 p(x,t\,|\,x_s) = s(x,t\,|\,x_s), \tag{1}$$

where $p(x, t\,|\,x_s)$ denotes the pressure field at position x, time t, and a source at x_s. The velocity model is represented by $c(x)$, and $s(x, t\,|\,x_s)$ is the source function. The solution to equation (1) is calculated by a finite-difference method (Levander 1988) and can be written in terms of its Green's function $g(x, t\,|\,x', 0)$ as

$$p(x,t\,|\,x_s) = \int g(x,t\,|\,x',0) * s(x',t\,|\,x_s)dx', \tag{2}$$

where the symbol * denotes temporal convolution. We can ignore the surface wave and shear wave effects in the elastic wave equation (Zhou *et al.* 1995) because the early arrivals in the 2D near surface seismic data contain few elastic effects.

EWI estimates the velocity model by minimizing the early arrival misfit function (Sheng *et al.* 2006; Boonyasiriwat *et al.* 2010), where the waveform data residual is defined as

$$\Delta p(x_g,t\,|\,x_s) = \left[p_{obs}(x_g,t\,|\,x_s) - p_{calc}(x_g,t\,|\,x_s) \right] W(x_g,t\,|\,x_s). \tag{3}$$

Here, x_g is the receiver position vector, p_{obs} and p_{calc} are, respectively, the observed and calculated pressure traces, and $W(x_g, t\,|\,x_s)$ is a window function that mutes all the energy except for the early arrivals. The velocity model $c(x)$ is iteratively updated by finding the slowness model that minimizes the misfit functional E, represented by the L_2 norm of the data residuals over time and space,

$$E = \frac{1}{2}\sum_s\sum_g\int\left(\Delta p(x_g,t\,|\,x_s)\right)^2 dt. \tag{4}$$

A non-linear conjugate-gradient method (Luo and Schuster 1991) is used to minimize the gradient function. The gradient of the misfit functional E with respect to changes in the velocity $c(x)$ is the first variation (Logan 1996) of E at the vector point $c(x)$ in the direction of $\delta c(x)$. This gradient $\left[grad(x) = \frac{\partial E}{\partial \delta c(x)} \right]$ is computed by migrating the waveform residuals (Tarantola 1984) with the following formula,

$$grad(x) = \frac{1}{c^3(x)}\sum_s\int \dot{p}_f(x,t\,|\,x_s)\,\dot{p}_b(x,t\,|\,x_s)dt, \tag{5}$$

where $\dot{p}$ is the time derivative of p, $p_f(x, t\,|\,x_s)$ represents the forward-propagated wavefields, and $p_b(x, t\,|\,x_s)$ represents the back-projected waveform residual wavefields given by

$$p_b(x,t\,|\,x_s) = \int g(x,-t\,|\,x',0) * \delta p(x',t\,|\,x_s)dx' \tag{6}$$

and

$$\delta p(x',t\,|\,x_s) = \sum_g \delta(x'-x_g)\Delta p(x_g,t\,|\,x_s). \tag{7}$$

Now the velocity model can be iteratively updated along the conjugate directions defined by

$$dk = -P_k g_k + \beta d_{k-1}, \tag{8}$$

where $k = 1, 2, …, k_{max}$, $g = [grad(x)]$, and P is the conventional geometrical-spreading preconditioner (Causse, Mittet and Ursin 1999). For the first iteration, we set $d_0 = -g_0$. The parameter β_k is calculated by the Polak-Ribiere formula (Nocedal and Wright 1999)

$$\beta_k = \frac{g_k^T\left(P_k - P_{k-1}g_{k-1}\right)}{g_{k-1}^T P_{k-1}g_{k-1}}, \tag{9}$$

and the velocity model is updated by

$$c_{k+1}(x) = c_k(x) + \lambda_k d_k(x), \tag{10}$$

where λ_k is the step length which can be determined by a quadratic line-search method (Nocedal and Wright 1999), and $d_k(x)$ is the component of the direction vector $d_k(x)$ indexed by x. To compute the gradient direction for each iteration reduces to computing the reverse time migration operation. Additional forward modellings are required for the line search. The initial velocity model $c_0(x)$ is the traveltime tomogram inverted by picked first arrivals (Nemeth, Normark and Qin 1997), and equation (10) is iteratively applied until the misfit functional E satisfies a stopping criterion.

Optimal frequency bands for MEWI

Since MEWI in the space-time domain uses a band of frequencies on each scale, it can update a much wider range of wave numbers than in the frequency domain (Boonyasiriwat *et al.*
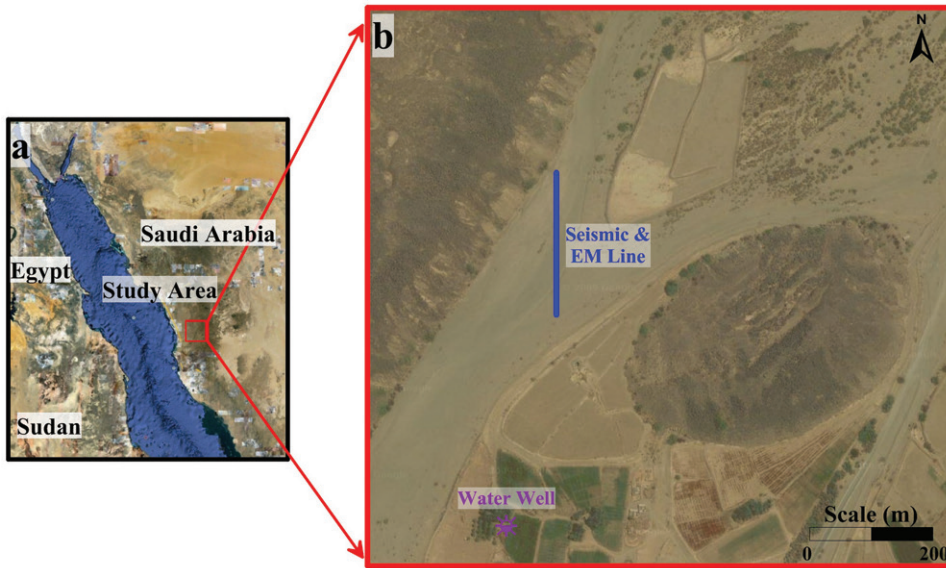
2010). The formula to select upscaling frequencies proposed by Sirgue and Pratt (2004) in the frequency domain is

$$f_{n+1} = \frac{f_n}{\alpha_{min}}, \tag{11}$$

where f_n is the current frequency, f_{n+1} is the next frequency to be chosen, and $\alpha_{min} = z / \sqrt{h^2 + z^2}$ is the parameter as a function of the maximum half offset h and the maximum depth z in the image. The vertical wave number range $[k_{z\,min}(f_n), k_{z\,max}(f_n)]$ is calculated by

$$k_{z\,min}(f_n) = \frac{4\pi f_n \alpha_{min}}{c_0}, \tag{12}$$

$$k_{z\,max}(f_n) = \frac{4\pi f_n}{c_0}, \tag{13}$$

where c_0 is the smooth background velocity model. Equation (11) guarantees that the lowest wave number to be updated at the $(n+1)$-th frequency f_{n+1} is equal to the highest wave number at the n-th frequency f_n. By equations (12) and (13), which are incorporated into equation (11), we obtain

$$k_{z\,min}(f_{n+1}) = k_{z\,max}(f_n). \tag{14}$$

In our work, we inherit this frequency selection strategy in the time domain to reduce the overlapped regions of recovered wave number components on two neighbouring scales. In time domain waveform inversion, a number of frequencies are used simultaneously for a given bandwidth. Here, we utilize equation (11) to choose f_n as the peak frequency for the frequency band on the n-th scale. Therefore, low-pass or bandpass filters with proper pass band and stop band windows can be applied to seismic data on different scales to control the recovered wave number range.

For a given frequency band, a grid size can be determined by the numerical stability and dispersion conditions associated with
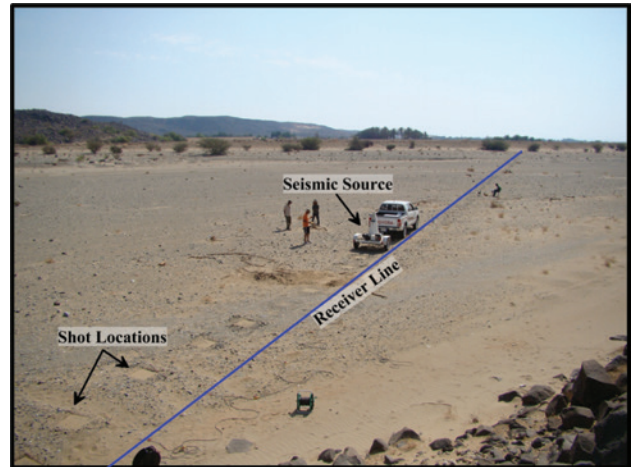

FIGURE 2

A photograph (looking south) taken during the data acquisition.

the finite-difference method on that scale. In this paper, the numerical dispersion condition for the finite-difference scheme is satisfied by more than ten grid points per dominant minimum wavelength (Levander 1988). A square grid with $d_x = d_z$ is applied. Once the space grid size is fixed, the time step dt can be determined by the 2D numerical stability condition (Courant, Friedrichs and Lewy 1928):

$$dt < \frac{dz}{\sqrt{2}c_{max}}, \tag{15}$$

where c_{max} is the maximum velocity.

ACQUISITION AND PROCESSING
Near surface refraction survey at Wadi Qudaid

The 2D seismic survey is conducted at Wadi Qudaid (see Fig. 1a) to the east of the campus of King Abdullah University of Science
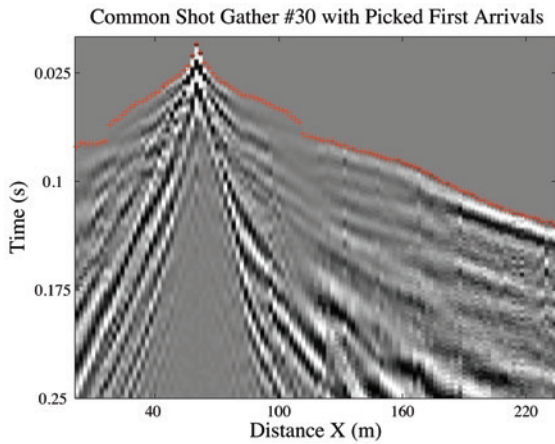
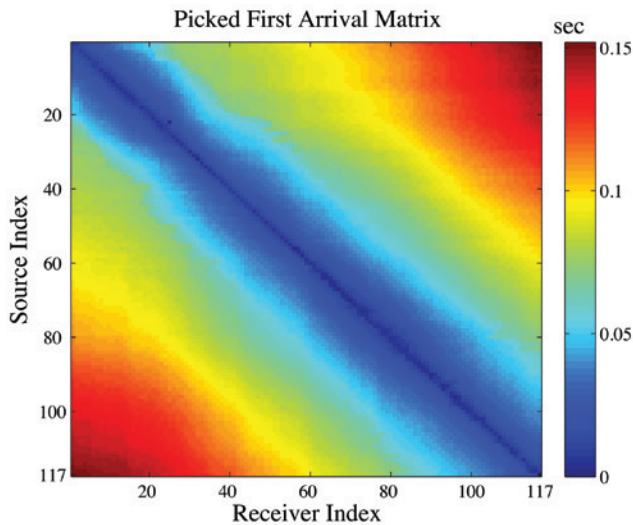FIGURE 3

CSG #30 with picked first arrival times.

FIGURE 4

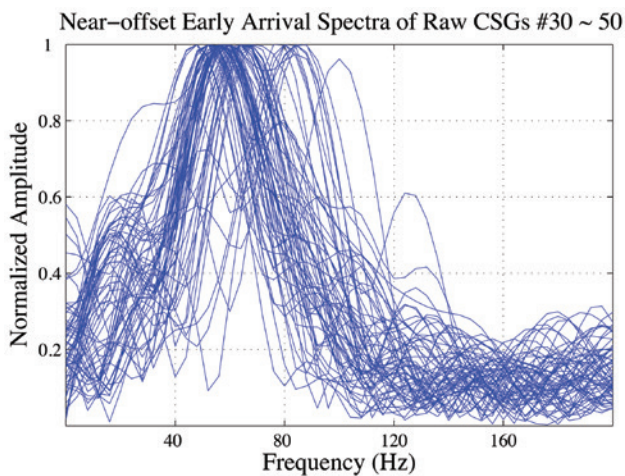The picked first arrivals for the wadi data set.

FIGURE 5

Near offset early arrival spectra of CSGs from #30 to #50.

and Technology (KAUST). The 2D acquisition geometry (Fig. 1b) consists of one line of vertical component geophones. Along this line, there are 117 receivers with a 2.0 m spacing, and the shots are located at every receiver position, so $117 \times 117 = 13\ 689$ traces are recorded. In this field experiment, we used a 200 lb weight drop (Fig. 2) to generate the seismic source energy with 10–15 stacks at each shot location. Each common shot gather (CSG) was recorded for 1 s with a sampling interval of 0.125 ms. Since we only need the early arrivals, arrivals after 0.25 s are muted. The CSG #30 and its picked first arrival traveltimes are shown in Fig. 3.

For this data set, we estimated the dominant wavelength and the dominant frequency of the first arrival head waves to be 6 m and 65 Hz, respectively, where the minimum P-wave velocity was estimated to be 380 m/s. Figure 4 shows the picked first arrival times for all traces presented as a 2D matrix, and Fig. 5 shows the early arrival spectra of near offset traces extracted from CSG #30 to CSG #50.

The land data are processed before applying MEWI in order to reduce elastic effects in the field data. The data processing steps include accounting for three-dimensional (3D) wave propagation effects, attenuation effects, trace normalization, extraction of the natural source wavelet, and bandpass filtering (Sheng *et al.* 2006. The following describes the detailed processing procedures.

Processing

1. The 3D land data are approximately transformed to 2D by multiplying the trace spectrum by $\sqrt{i/\omega}$ in the frequency domain and by multiplying the trace by $\sqrt{t}$ in the time domain (Boonyasiriwat *et al.* 2010).

2. The attenuation effects in the field data should be corrected for because the forward modelling is based on the acoustic wave equation. According to Liao and McMechan (1997), the linear attenuation transfer function T is a function of f, t and Q, such that

$$T(f) = e^{-\left(f\frac{\pi t}{Q}\right)},\tag{16}$$

which transforms the input first arrival signal spectrum $S(f)$ to the output trace spectrum $R(f)$ by $R(f) = T(f)S(f)$. In equation (16), f represents the frequency corresponding to the horizontal axis of the data spectrum, and t is the first-arrival traveltime. Divided by the factor $T(f)$, the attenuation in the recorded data spectrum $R(f)$ can be compensated and transformed into S(f) using equation (16). In this study, Q is fixed for the early arrivals, and is also assumed independent of f. The factor Q can also be written in terms of the centroid frequencies f_r and f_s of the first arrival at the receiver and the source, respectively, as

$$f_r = f_s - \frac{2\pi\sigma_s^2}{Q}t,\tag{17}$$

where σ_s^2 represents the variance of the source spectrum. After f_r, f_s and σ_s^2 are estimated from the data and the first arrivals t

are picked, the Q value can be estimated from equation (17). Then equation (16) is applied to the traces to correct the attenuation effects in the frequency domain. In this work, we estimate Q to be a constant because we only deal with early arrivals coming from a shallow part of the earth. Thus the same attenuation correction formula is used for all the traces.

3. All traces are normalized to reduce the errors resulting from previous correction steps. To retain only the early arrivals, the traces are also muted with a time window that starts about three to four periods after the first arrival. In this case, surface waves and later arrivals are not inverted by MEWI.

4. To enhance the MEWI results, a natural source wavelet is extracted by averaging the near offset first arrivals within a window of 10–20 traces. We apply zero-lag cross correlation to several consecutive traces to align them to their first arrivals. Figure 6(b) shows the calculated natural source wavelet using the rectangular window (Fig. 6a) to catch the first arrival wavelets for CSG #25 after the attenuation correction. Since the weight drop is controlled electronically, all shots have similar source wavelets as illustrated by Fig. 7.

5. The very near offset traces with source-receiver offsets no greater than 14 m are muted because they contain surface waves and noise even after filtering, and it is difficult to match them with the calculated seismograms. Noise before the picked first arrivals is also muted.

6. In the recorded wadi data set whose average peak frequency of the early arrivals is estimated to be 65 Hz, the initial filtered data for MEWI have a peak frequency of $f_1 = 18$ Hz because most noise and surface waves are under 10 Hz in this data set. In our field experiment, we estimated the depth $z = 70$ m and the maximum half offset $h = 116$ m, which leads to $f_2 = 0.52$ by $\alpha_{min} = z/\sqrt{h^2 + z^2}$. According to equation (11),

we set $f_2 = 34$ Hz and $f_3 = 65$ Hz as the peak frequencies for the next two stages of MEWI. Therefore, three bandpass filters with sequentially growing pass bands 0~25 Hz, 0~45 Hz and 0~75 Hz are respectively applied to all the traces on three different scales. These filters are also applied to the extracted source wavelet in step 4 such that MEWI can be conducted on each scale with an appropriate source.

NUMERICAL TESTS
MEWI velocity inversion

Figure 8 shows the centroid frequencies f_r plotted against traveltimes of the first arrivals. The variance σ_s^2 of the source centroid spectra is equal to 312.70 Hz^2, which is the average σ_s^2 value

FIGURE 7

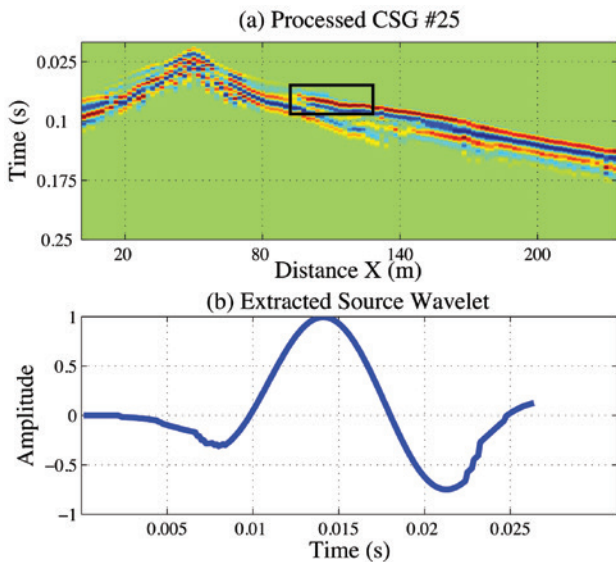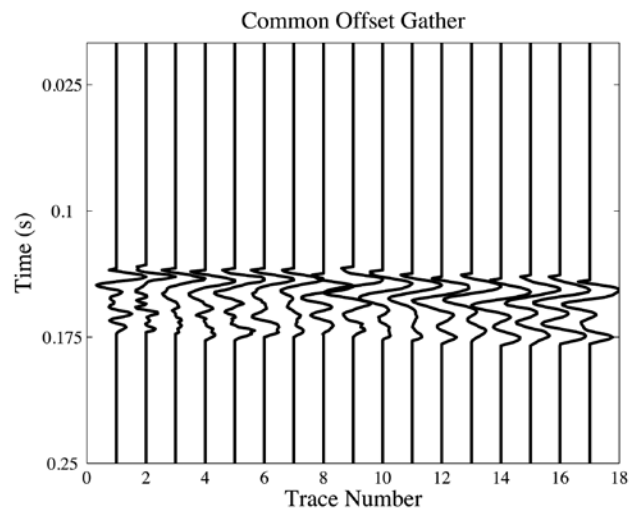Common offset gather with an offset equal to 200 m.

FIGURE 6

(a) The processed (steps 1~5) CSG #25 after the application of a muting window and (b) the source wavelet extracted from the early arrivals.
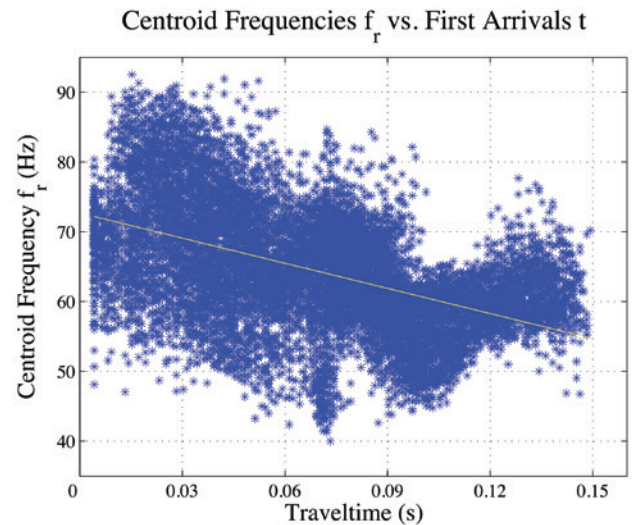

FIGURE 8

Pairs of the centroid frequencies and the first arrival traveltimes at the receivers. The attenuation factor Q is estimated to be 28 by the best-fit line denoted by the solid yellow line.
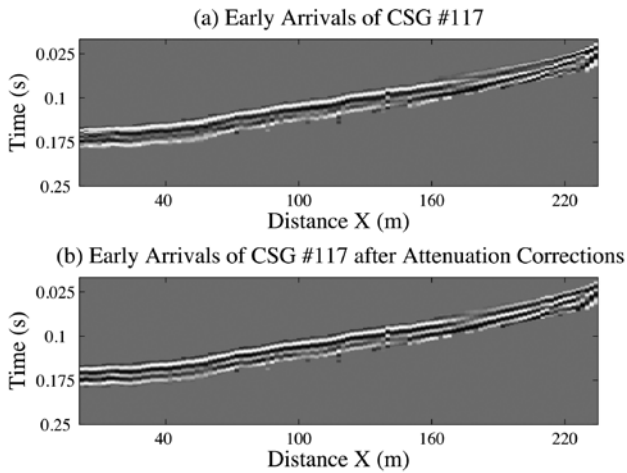
FIGURE 9

(a) The original and (b) the Q corrected (bottom) early arrivals of CSG #117.
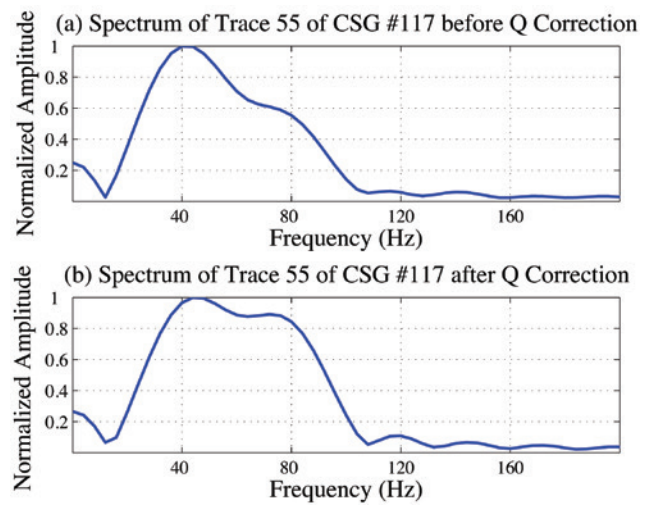

FIGURE 10

Spectrum comparisons (a) before and (b) after the attenuation correction.
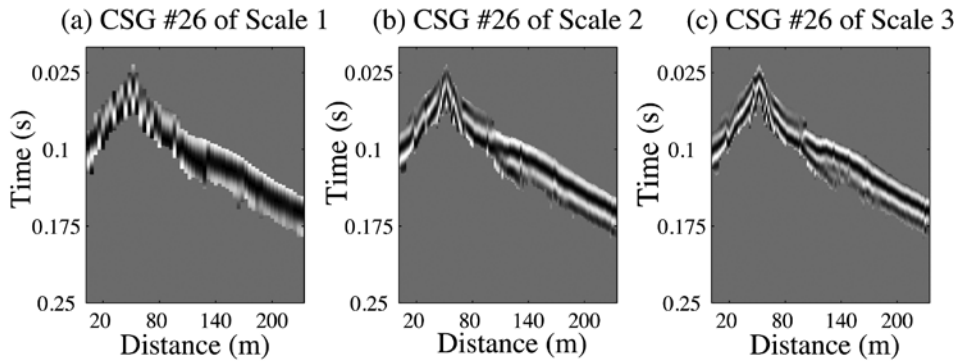

FIGURE 11

Processed CSG #26 used for MEWI on (a) the coarsest, (b) the intermediate and (c) the finest scales.
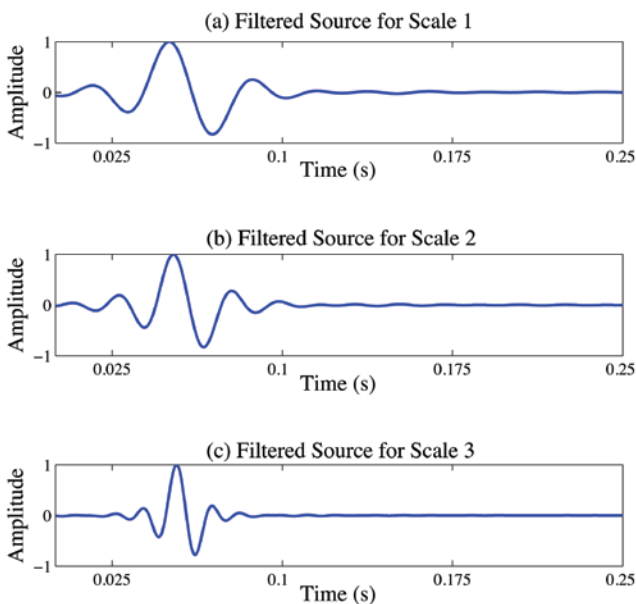

FIGURE 12

Filtered source wavelets used for MEWI on (a) the coarsest, (b) the intermediate and (c) the finest scales.

from all the sources (Liao and McMechan 1997). Here, since the dominant peak frequency of the collected data is 65 Hz, we use a sub-band of 25–90 Hz to calculate f_r, f_s and σ_s^2 to avoid errors from the noise. By equation (17), the Q value is estimated to be about 28, which is a typical value for near surface soil with significant absorption. According to equation (16), $1/T(f)$ is applied to the trace spectra to correct for the attenuation effects in the frequency domain. Figure 9 shows CSG #117 before and after the attenuation correction, and Fig. 10 demonstrates the spectrum comparisons of one trace before and after this operation. Figure 11 presents the raw and corrected CSG #26 before and after all the processing steps for three different scales. Figure 12 depicts three filtered source wavelets based on the extracted wavelet (see Fig. 6b) for MEWI.

Figure 13(a) exhibits the smoothed traveltime tomogram which is used as the initial velocity model for MEWI on the coarsest scale. Similarly, the tomogram inverted on the n-th scale is used as the initial velocity model on the $(n+1)$-th scale. We set the spatial grid size $dx = 4$ m, 2 m and 1 m for the coarsest, intermediate and finest scales, respectively. The sampling interval dt is equal to 0.125 ms and the total number of time steps is 2000. On the coarsest scale, we use 58 CSGs (all the even numbered CSGs)

instead of 117 CSGs to accelerate the computation by matching fewer data, while all the CSGs are used on the other two upscales. When conducting MEWI, for the coarsest scale, we choose p_f and p_b instead of $\dot{p}_f$ and $\dot{p}_b$ in equation (5) to calculate the gradient by utilizing the low-frequency data. On the intermediate scale, we take the time derivative on either p_f or p_b. Then we gradually turn to using $\dot{p}_f$ and $\dot{p}_b$ on the finest scale to attach more importance to high-frequency components in the data.

Figure 13(b–d) shows the inverted tomograms by MEWI on different scales. Compared to the traveltime tomogram, MEWI iteratively generates tomograms with gradually increasing resolutions by sequentially matching the collected data from low to high frequencies. In Fig. 14, the processed CSG #116 are compared with the calculated data by MEWI on each scale. Many early arriving events in the synthetic data correlate well with the observed traces in Fig. 14(a–c). From the tomogram on the finest scale, we also estimate a water table curve according to the velocity contour of 1550 m/s. Relying on this curve, the esti-

mated water table in the MEWI tomogram is generally consistent with, but 9% deeper than in, the traveltime tomogram, showing that the water storage in this wadi might be less than expected from the traveltime tomogram. A well log reference of geological conditions above the 18 m deep water table is shown in Fig. 15. The first layer (Fig. 15a) consists of loose sand with gravels, and the second layer (Fig. 15b) consists of compact sand with some gravel and partially to fully saturated with water.

Sanity test on synthetic data
In order to illustrate the effectiveness of EWI, we also conduct synthetic tests. The synthetic data set is generated based on the final velocity tomogram inverted by MEWI on the finest scale, as shown in Fig. 16(a). The first arrival traveltimes of this synthetic data set are automatically picked and inverted by the traveltime tomography. The resulting traveltime tomogram is presented in Fig. 16(b). Compared to the original traveltime tomogram in Fig. 13(a), they match well in the 2D subsurface
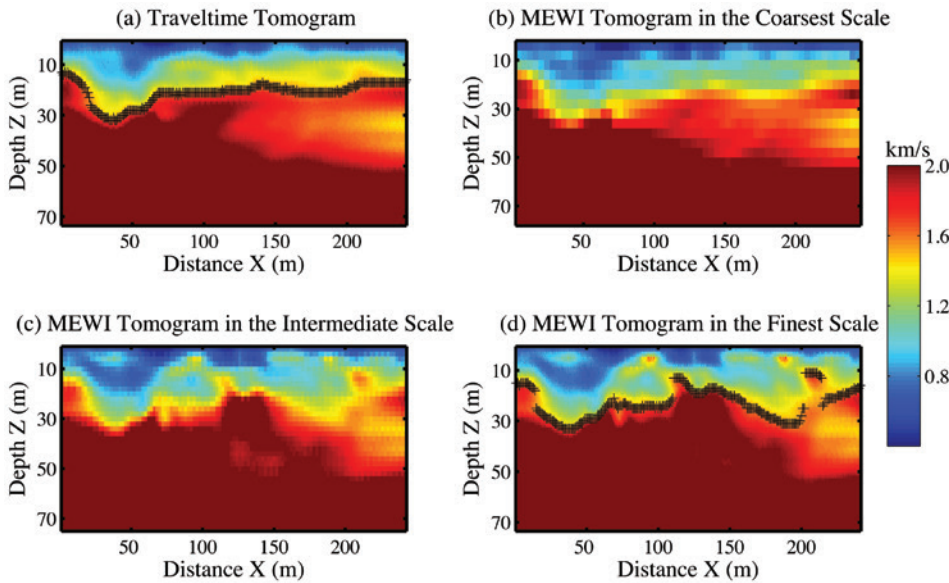

FIGURE 13
(a) The traveltime tomogram, and the MEWI tomograms on (b) the coarsest, (c) the intermediate and (d) the finest scales. The contours on (a) and (d) marked by the black crosses indicate the velocity at 1550 m/s, which is that of the bedrock.
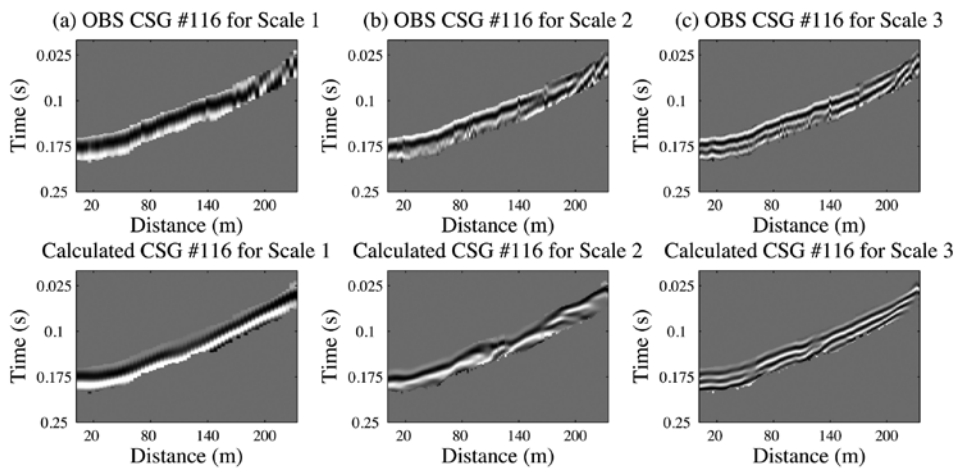

FIGURE 14
Comparisons of the processed observed CSG #116 and calculated CSG #116 on (a) the coarsest, (b) the intermediate and (c) the finest scales.
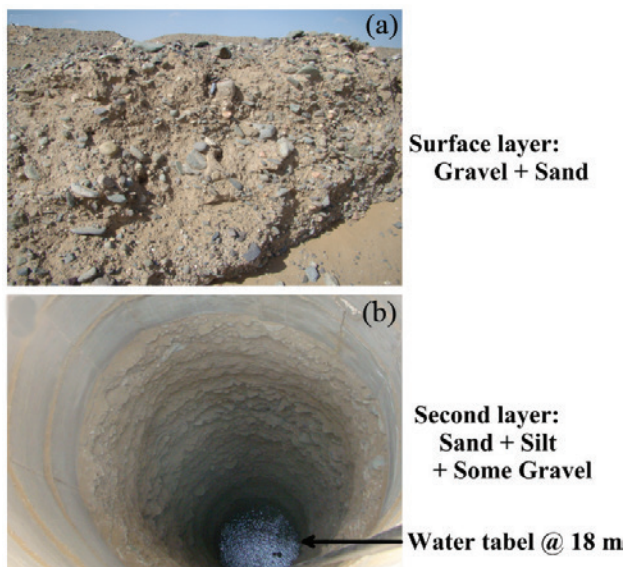
FIGURE 15

Two photographs show the subsurface layers: (a) the first layer composed of gravel and sand, with a thickness less than 5 m. (b) The second layer as shown inside a water well near the study area (Fig. 1b). It is composed of sand and silt with some gravel and has a thickness of 10–15 m.

FIGURE 16

Sanity test on a synthetic example, an application of EWI to the early arrival data generated by the MEWI tomogram. (a) The true velocity model (Fig. 13d), (b) the traveltime tomogram and (c) the EWI tomogram.

space. It is not necessary to carry out attenuation corrections for this synthetic data set since it is computed by a finite-difference solution to the acoustic wave equation. We then apply EWI using this new traveltime tomogram as the initial velocity model by keeping the same size early arrival window as in the MEWI. Figure 16(c) shows the tomogram inverted by EWI after 30 iterations. It shows highly resolved subsurface structures compared to the traveltime tomogram and validates EWI's capability for improved resolution compared to traveltime tomography.

CONCLUSIONS

The MEWI method is used to invert seismic data collected at Wadi Qudaid. Compared to traveltime tomography, MEWI does not require a high-frequency assumption and benefits from the attenuation correction applied to the recorded traces. MEWI can be successfully applied to near surface seismic data if careful processing steps are carried out before inversion. These steps include a low-pass or bandpass filter and corrections for 3D geometric spreading and attenuation effects, trace normalization, and accurate estimation of the source wavelet. Our synthetic and field data results suggest that MEWI can create a more accurate and highly resolved velocity model compared to the traveltime tomogram. For reflections events from deep reservoir geology in the oil industry, it is necessary to dynamically widen the early arrival window or invert the deep reflections. Recall, it is important to recognize that EWI is designed to work well if the diving waves are in the early arrival window, and so the tomogram depth is limited to the diving wave's depth of penetration. This is the main reason that MEWI can be applied to inverting for shallow subsur-
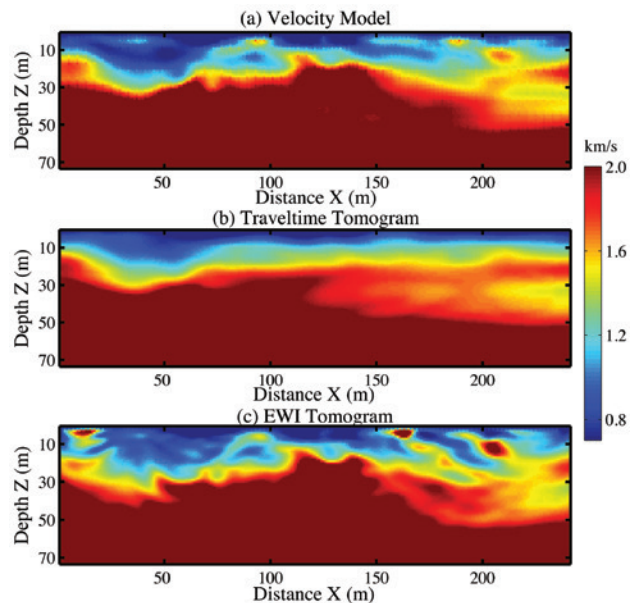
face structures of the earth. Otherwise it is necessary to dynamically open the arrival window to invert for the deeper reflections.

The drawbacks of MEWI compared to traveltime tomography include complicated data processing steps and higher computational cost. Moreover, MEWI fits complex waveforms instead of arrival times, which can be prone to cycle skipping and getting stuck in a local minimum, although low-frequency data are first used in the inversion.

REFERENCES

Aki K. and Richards P.G. 2002. *Quantitative Seismology*, 2nd edition. University Science Books.

Boonyasiriwat C., Schuster G.T., Valasek P. and Cao W. 2010. Applications of multiscale waveform inversion to marine data using a flooding technique and dynamic early-arrival windows. *Geophysics* **75**, R129–R136.

Buddenseik M. 2004. *Colluvial wedge imaging using traveltime tomography along the wasatch fault near mapleton*. Master thesis, Utah.

Bunks C., Saleck F.M., Zaleski S. and Chavent G. 1995. Multiscale seismic waveform inversion. *Geophysics* **60**, 1457–1473.

Causse E., Mittet R. and Ursin B. 1999. Preconditioning for full-waveform inversion in viscoacoustic media. *Geophysics* **64**, 130–145.

Courant R., Friedrichs K.O. and Lewy H. 1928. Über die partiellen Differenzengleichungen der mathematischen Physik. *Mathematische Annalen* **100**, 32–74.

Levander A.R. 1988. Fourth-order finite-difference p-sv seismograms. *Geophysics* **53**, 1425–1437.

Liao Q. and McMechan G.A. 1997. Tomographic imaging of velocity and q, with application to crosswell seismic data from the gypsy pilot site, Oklahoma. *Geophysics* **62**, 1804–1811.

Logan J.D. 1996. *Applied Mathematics*, 2nd edition. Wiley-Interscience.

Luo Y. and Schuster G.T. 1991. Wave equation traveltime inversion. *Geophysics* **56**, 645–653.

Marfurt K.J. 1984. Accuracy of finite-difference and finite-element modeling of the scalar and elastic wave-equations. *Geophysics* **49**(5), 533–549.

Mora P.R. 1987. Nonlinear two-dimensional elastic inversion of multi-off-set seismic data. *Geophysics* **52**, 1211–1228.

Nemeth T., Normark E. and Qin F. 1997. Dynamic smoothing in crosswell traveltime tomography. *Geophysics* **62**, 168–176.

Nocedal J. and Wright S.J. 1999. *Numerical Optimization*. Springer series in operations research and financial engineering.

Nolet G. 1987. *Seismic Tomography*. Springer.

Pratt R.G. and Goulty N.R. 1991. Combining wave-equation imaging with traveltime tomography to form high-resolution images from crosshole data. *Geophysics* **56**, 208–224.

Pratt R.G., Shin C. and Hicks G.J. 1998. Gauss-newton and full Newton methods in frequency space seismic waveform inversion. *Geophysical Journal International* **133**, 341–362.

Sheng J., Leeds A., Buddenseik M. and Schuster G.T. 2006. Extending the aperture and increasing the signal-to-noise ratio of refraction surveys with super-virtual interferometry. *Geophysics* **71**, U47–U57.

Sirgue L. and Pratt R.G. 2004. Efficient waveform inversion and imaging: A strategy for selecting temporal frequencies. *Geophysics* **69**, 231–248.

Song Z.M. and Williamson P.R. 1995. Frequency-domain acoustic-wave modeling and inversion of crosshole data: Part I 2.5-d modeling method. *Geophysics* **60**(3), 784–795.

Tarantola A. 1984. Inversion of seismic reflection data in the acoustic approximation. *Geophysics* **49**, 1259–1266.

Zhou C., Cai W., Luo Y., Schuster G.T. and Hassanzadeh S. 1995. Acoustic wave-equation traveltime and waveform inversion of crosshole seismic data. *Geophysics* **60**, 765–773.

Zhou C., Schuster G.T., Hassanzadeh S. and Harris J.M. 1997. Elastic wave equation traveltime and waveform inversion of crosswell data. *Geophysics* **62**, 853–868.

Zhu X. and McMechan G.A. 1989. Estimation of a two-dimensional seismic compressional-wave velocity distribution by iterative tomographic imaging. *International Journal of Imaging System and Technology* **1**, 13–17.